

Evaluation of the Skeletal Kinetics of Fluorine-18-Fluoride Ion with PET

Randall A. Hawkins, Yong Choi, Sung-Cheng Huang, Carl K. Hoh, Magnus Dahlbom, Christiaan Schiepers, Nagichettiar Satyamurthy, Jorge R. Barrio, and Michael E. Phelps

Division of Nuclear Medicine and Biophysics, Department of Radiological Sciences, Laboratory of Nuclear Medicine (DOE), Laboratory of Biomedical and Environmental Sciences, and The Crump Institute for Biological Imaging, UCLA School of Medicine, University of California, Los Angeles, California*

To evaluate the feasibility of quantitatively assessing regional skeletal fluoride uptake in humans in focal and generalized bone disease, we investigated the skeletal kinetics of [^{18}F]fluoride ion with dynamic PET imaging. Dynamic image sets were acquired over a 60-min interval in a multiplane PET device, and input functions (plasma ^{18}F time-activity curves) were measured directly from arterialized blood and, in some cases, determined from image-derived left ventricular cavity activity measurements. Our results indicate:

1. A steady-state ratio of [^{18}F]fluoride ion concentration in plasma to whole blood greater than unity (1.23 for plasma to directly assayed whole blood and 1.44 for plasma to left ventricular cavity imaged concentrations. This concentration difference produces a scaling factor that must be considered when using image derived or directly measured input functions.
2. The preferred tracer kinetic model configuration for [^{18}F]fluoride ion skeletal kinetics is a three compartment model that includes a "bound" and "unbound" bone [^{18}F]fluoride ion compartment.
3. The rate constant for forward transport of [^{18}F]fluoride ion from plasma to the extravascular space of bone (K_1) and the regional blood volume parameter generate estimates of bone blood flow and vascular volume, respectively, that are in the physiologic range of reported for mammals. Estimates of the uptake constant for fluoride in bone, using nonlinear regression ($K_{\text{NLR}} = 0.0360 \pm 0.0064$ ml/min/ml), are in very good agreement with an estimate of the same parameter obtained with Patlak graphical analysis ($K_{\text{PAT}} = 0.0355 \pm 0.0061$ ml/min/ml).
4. Generating parametric images of K_{PAT} facilitates quantification of regional bone [^{18}F]fluoride ion kinetics.

The method is computationally practical, and, with either the parametric imaging approach or with standard region of interest analysis, can be used to generate quantitative estimates

of fluoride uptake (a "bone metabolic index") in focal skeletal regions or in more generalized distributions.

J Nucl Med 1992; 33:633-642

The skeletal system is in a state of dynamic equilibrium between bone formation and resorption. Bone-seeking radiopharmaceuticals have been used for many years primarily to image the relative distribution of bone metabolic activity as a clinical indicator of focal disease (including neoplasms, trauma, and infections) and, to a lesser extent, to quantitatively evaluate bone metabolic characteristics, both in focal and generalized bone disease. Virtually all clinical bone scans are performed with $^{99\text{m}}\text{Tc}$ -methylene diphosphonate (MDP) compounds with gamma camera systems. Quantitative methods to estimate absolute indices of MDP uptake and retention in bone as an indicator of generalized bone metabolism have been developed and applied in metabolic disorders such as hyperparathyroidism, both with planar imaging and SPECT techniques (1-4).

It was our purpose in this work to develop a quantitative technique for evaluating skeletal metabolism with the bone-seeking tracer [^{18}F]fluoride ion and dynamic PET imaging. Because of more accurate attenuation correction methods and other factors, most PET systems produce more quantitatively precise volumetric measurements of activity concentrations than SPECT systems. It was our goal to develop a tracer kinetic model appropriate for dynamic PET [^{18}F]fluoride ion studies that produces a kinetic description of fluoride dynamics that may be applicable to focal and generalized bone diseases.

Fluorine-18-fluoride ion was at one time the standard bone scanning agent. Bone scanning with [^{18}F]fluoride ion was first introduced by Blau et al. (5), and further basic and clinical evaluations of the method followed (6-13). Fluorine-18-fluoride ion was, in fact, fully approved by the FDA for clinical use. Technetium-99m-diphosphonate compounds supplanted ^{18}F for bone scanning in the 1970s because of the more optimal physical characteristics of

Received Jun. 28, 1991; revision accepted Dec. 4, 1991.

For reprints contact: Randall A. Hawkins, MD, PhD, Division of Nuclear Medicine and Biophysics, Department of Radiological Sciences, UCLA School of Medicine, 10833 Le Conte Ave., Los Angeles, CA 90024-1721.

* Operated for the U.S. Department of Energy by the University of California under contract DE-FC03-87ER60615.

^{99m}Tc compounds for gamma camera studies. Fluorine-18-fluoride ion is, however, an excellent bone imaging agent that is extracted by the skeletal system in proportion to bone blood flow and osteoblastic activity in a manner qualitatively similar to the mechanism of uptake of ^{99m}Tc -diphosphonate compounds.

Investigators have previously studied the kinetics of [^{18}F]fluoride ion in bone with plasma clearance and tissue sampling techniques in animals (14,15) and plasma clearance methods alone in humans (16,17). Reeve, Wooton and colleagues demonstrated that plasma clearance estimates of [^{18}F]fluoride ion kinetics produce useful indices for monitoring the response of Paget's disease to calcitonin therapy (16) and, more recently, found that [^{18}F]fluoride ion bone uptake, which they relate to bone blood flow with a tracer kinetic model, correlated with the work rate of osteoblasts in idiopathic or postmenopausal osteoporosis (17).

In this work, we have investigated tracer kinetic models for [^{18}F]fluoride ion skeletal uptake, similar to those originally proposed by Charkes and colleagues (14,18,19) from theoretical considerations and animal tissue sampling studies, but using a modern multiplane PET tomograph, in normal subjects and in one cancer patient.

MATERIALS AND METHODS

Preparation of [^{18}F]Fluoride Ion

Fluorine-18-fluoride ion was produced using a method reported by Wieland et al. (20). The target (300 μl of H_2^{18}O) was irradiated with 10.5 MeV protons (20 μA for 10 min). At the end of bombardment, the activity (about 125 mCi) was automatically transferred to a vial containing normal saline (10 ml). The solution was sterilized by passing it through a Millipore filter (0.22 μmol) into a sterile multidose vial.

Human Subjects

Eleven healthy male volunteers, ages 23 to 59, and one breast cancer patient were studied after granting informed written consent. The experimental protocol was approved by the UCLA Human Subject Protection Committee. The breast cancer patient was studied on three separate occasions.

Image Acquisition

Separate intravenous lines were placed in a dorsal vein of each hand for injections of [^{18}F]fluoride ion and for plasma sampling, respectively. About 5–10 mCi of [^{18}F]fluoride ion diluted in 10 ml saline solution was injected over 30 sec. The intravenous line was then flushed with an additional bolus of 10 ml saline given over a 30-sec interval.

Image acquisition was initiated simultaneously with [^{18}F]fluoride ion injection and consisted of a dynamic sequence of thirty 120-sec frames (in Volunteers 1–8, Table 1 A and B, and in the first study of the breast cancer patient) or twelve 10-sec, four 30-sec, and twelve 240-sec frames (in Volunteers 9–11 and in the second and third study of the breast cancer patient, Tables 1 A - B and 2) for a total imaging time of about 1 hr. All studies were performed on a Siemens/CTI 931/08-12 tomograph. This device produces 15 simultaneous imaging planes encompassing a 108-mm axial field of view. The 15-plane image sequence was ac-

quired over the mid-thoracic spine in order to include the heart in the field of view. In the more rapid initial image acquisitions, including the heart in the field of view permits generation of the input function directly from the image data (21,22).

Fifteen plane cross-sectional dynamic images were reconstructed employing a Shepp-Logan filter with a cut-off frequency of 0.3 Nyquist frequency, yielding a spatial resolution of ~ 10 mm FWHM in plane. Photon attenuation was corrected using a 20-min transmission scan obtained with a $^{68}\text{Ge}/^{68}\text{Ga}$ external ring source.

Blood Sampling

Plasma input curves were obtained from a vein heated to 43°C to arterialize the venous blood (23). About 25 2-ml blood samples were obtained in each study. The blood sampling frequency was approximately every 10 sec for the first 3 min after [^{18}F]fluoride ion injection, and at progressively longer intervals for the duration of the imaging period. All blood samples were heparinized and placed on ice immediately upon withdrawal. Samples were then centrifuged and the plasma fraction separated for measurement of ^{18}F count rates. In five subjects, additional blood samples (at about 10–30-sec intervals initially and at 10–15-min intervals for the duration of the study) were obtained in order to determine the distribution of [^{18}F]fluoride ion between plasma and whole blood as a function of time.

A cylindrical phantom (20 cm diameter) containing $^{68}\text{Ge}/^{68}\text{Ga}$ was scanned before each study and a known volume of $^{68}\text{Ge}/^{68}\text{Ga}$ from the cylinder was counted in the well counter to obtain a conversion factor between image data in units of cts/pixel/sec and well counter data in units of cts/ml/sec.

Plasma fluoride (unlabeled) concentrations were measured (Mayo Clinic, Rochester, MN) in three normal subjects and in the second and third studies on the breast cancer patient.

Mathematical Model

Fluoride ion is rapidly cleared from the plasma both through renal excretion and by diffusion through capillaries with eventual incorporation into bone. Fluoride ion exchanges with hydroxyl groups in the hydroxyapatite crystal of bone ($\text{Ca}_{10}(\text{PO}_4)_6\text{OH}_2$) to form fluoroapatite ($\text{Ca}_{10}(\text{PO}_4)_6\text{F}_2$) (12,24).

While we evaluated several different possible model configurations for fluoride ion incorporation into bone, the two models in best agreement (fit) with the data, that also are consistent with the known biological distribution of fluoride ion, are a simple two-compartment model, consisting of a vascular (plasma) compartment and a bone compartment, and a three-compartment model (Fig. 1), consisting of a vascular compartment, an extravascular compartment (C_e) and a compartment of bound fluoride (C_b). This model configuration is similar to that previously proposed by Charkes et al. (14,18,19) although, because our model

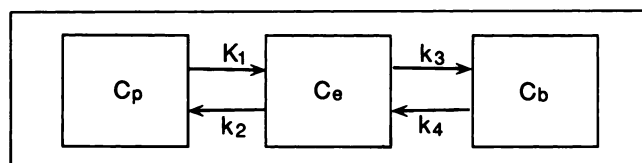


FIGURE 1. Three-compartment model of skeletal [^{18}F]fluoride ion kinetics. C_p , C_e and C_b refer, respectively, to the plasma, extravascular and bound bone compartments. K_1 , k_2 , k_3 and k_4 are first-order rate constants describing the potential directional exchanges between compartments.

is a regional tracer kinetic model as opposed to Charkes' whole-body pharmacokinetic model, it does not include a renal compartment or a total-body extracellular space compartment.

Physiologically, C_e represent [^{18}F]fluoride ion in an extravascular space unbound to bone, while C_b refers to the activity bound to bone (either on the bone surface or fully incorporated into the hydroxyapatite crystal). Rate constants describing the transport between the compartments include K_1 and k_2 for forward and reverse transport from plasma for the two-compartment model and K_1 , k_2 (forward and reverse transport) and k_3 and k_4 (incorporation and release from the bound compartment C_b) for the three-compartment model.

Both the two- and three-compartment models have been utilized in a variety of tracer kinetic studies with PET. For example, the two compartment model has been used with ^{68}Ga EDTA for blood-brain barrier diffusion kinetic studies (25), and the three-compartment model for the well known 2- ^{18}F fluoro-2-deoxy-D-glucose (FDG) model of glucose metabolism in the brain and heart (23,26,27). Data analysis methods and computational methods employed for parameter estimation using these models have been previously described (23,27,28).

In addition to the individual model rate constants (microparameters) described above, an additional parameter of interest in the three-compartment model is the macroparameter K_{NLR} (where the subscript NLR refers to K determined by nonlinear regression), defined by:

$$K_{\text{NLR}} = \frac{K_1 k_3}{k_2 + k_3} \text{ (ml/min/ml).} \quad \text{Eq. 1}$$

Analogously to the FDG model (23,26), the net transport of fluoride from plasma into bone is defined by the expression:

$$\text{Fluoride transport} = K[F] \text{ (nmol/min/ml),} \quad \text{Eq. 2}$$

where K is defined by Equation 1 or Equation 5 (below) and $[F]$ is the plasma concentration of fluoride (unlabeled). Therefore, if K is measured kinetically and the plasma fluoride concentration is measured directly, the mass fluoride transport flux can be determined with Equation 2.

The turnover half-times of the extravascular (C_e) and bound compartments C_b , are given by:

$$t_{1/2}(C_e) = 0.693/(k_2 + k_3) \quad \text{Eq. 3}$$

$$t_{1/2}(C_b) = 0.693/k_4. \quad \text{Eq. 4}$$

Because the net uptake of [^{18}F]fluoride ion from plasma to bone lattice is primarily unidirectional over the time period of observation in this study (see Results), the Patlak graphical method (29,30) can be employed to determine the macroparameter K defined in Equation 1 (designated K_{PAT} when determined in this manner) either regionally, or pixel by pixel to generate parametric images of K_{PAT} , as previously shown by our group for myocardial glucose utilization parametric images (21).

In this method, K_{PAT} is determined with the following expression:

$$C_i(T)/C_p(T) = K_{\text{PAT}} \int_0^T C_p(t)dt/C_p(T) + V, \quad \text{Eq. 5}$$

where $C_i(T)$, which is equal to the sum of $C_e(T)$ and $C_b(T)$ for the three-compartment model, is the measured bone tissue activity concentration at time t ; $C_p(T)$ is the plasma input function at time T ; and V is related to the effective distribution volume of

the tracer. K_{PAT} is estimated from the slope of the graph, $C_i(T)/C_p(T)$ vs. $[\int_0^T C_p(t)dt]/C_p(T)$ assuming k_4 is equal to zero.

Data Analysis

Each dynamic image acquisition set generated a series of transaxial images at 15 planes through the patient. The thoracic spine was included in the field of view in each image, and regions of interest (ROIs) were selected over the vertebral body in each image of each dynamic set. The vertebral body represented the largest identifiable focus of bone within the field of view of each image. While the neural arch, transverse and spinous processes were clearly visible in the images, only regions over the vertebral bodies were used for analysis in the normal controls. In the cancer patient, additional ROIs were constructed corresponding to focal metastatic disease characterized by zones of increased [^{18}F]fluoride ion uptake.

The 15 image planes of each dynamic sequence were equally separated spatially (slice thickness 6.75 mm), but were not fixed in relation to vertebral bodies and disk interspaces. In those slices near or through a vertebral disk, the low or absent uptake of ^{18}F in the disc substance caused a significant diminution of count densities in the vertebral body region. However, because of partial volume averaging of signal from the adjacent bone into the disk space, it was still possible to define "vertebral body" ROIs in most image planes 150 out of 165 image planes in 11 normal subjects).

In the three subjects with rapid initial scan sequences, ROIs in the left ventricular cavity were drawn on images that best represented the ventricular activity. In each subject, a single scan level was chosen for generating the left ventricular input function.

RESULTS

Fluorine-18-Fluoride Ion Distribution Between Plasma and Whole Blood

Figure 2 illustrates a typical input function obtained from arterialized venous plasma, whole blood and from a ROI over the left ventricle in a subject who underwent the rapid initial scanning sequence. Note the consistently

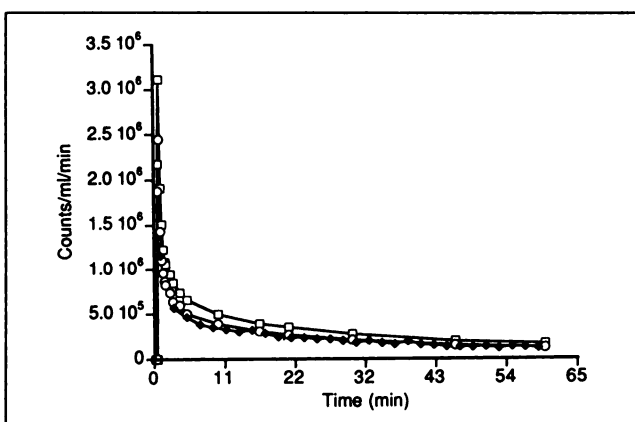


FIGURE 2. Representative input function from a normal volunteer. Data obtained from heated plasma samples (open squares), whole blood (open circles) and left ventricular ROIs (filled diamonds) are shown.

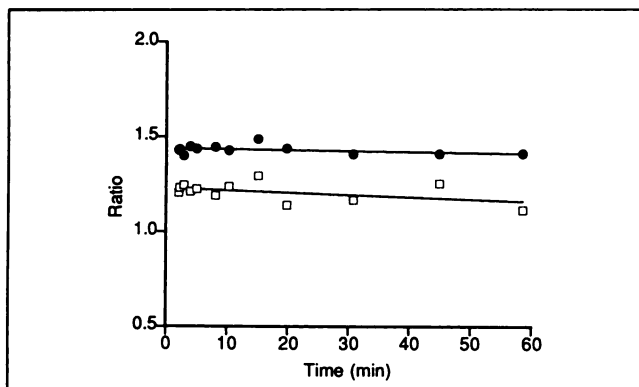


FIGURE 3. Plot of plasma [^{18}F]fluoride ion concentrations versus left ventricular activity concentrations (P/LV, filled circles) and plasma ^{18}F concentrations versus whole blood activity values (P/WB, open rectangles). Linear regression resulted straight lines as shown through data points, y-intercepts: 1.44 for P/LV, 1.23 for P/WB. Both lines have a slight, but statistically significant negative slope: 0.00045 for P/LV, 0.00123 for P/WB).

higher plasma concentrations as compared to whole blood and left ventricular concentrations of ^{18}F .

Figure 3 contains a plot of the ratios of average plasma ^{18}F concentrations determined from plasma samples to left ventricular concentrations determined from images, as a function of time, in 11 normal subjects. Additionally, a plot of the ratio of plasma activity to measured whole blood activity in four normal subjects is illustrated. Linear regression analysis applied to both sets of data yielded an initial ratio (i.e., at $t = 0$) of 1.44 for plasma-to-left ventricular counts and 1.23 for plasma-to-whole blood counts. As illustrated in Figure 3, the ratios were fairly constant, although a slight decline as a function of time was evident.

Comparison of Two-Compartment Versus Three-Compartment Model

The choice of a model configuration for a given data set is determined by a variety of factors, including biochemical and physiologic supporting data and statistical analysis. An effective operational approach is to select a model with the fewest number of parameters that adequately fits the data, while maintaining a biologically relevant model configuration (31).

One useful statistical test for determining whether a model configuration with more parameters significantly improves the statistical quality of the model fit is a method using the F statistic, defined by:

$$F = \frac{(RSS_1 - RSS_2)/(P_2 - P_1)}{RSS_2/(N - P_2)}, \quad \text{Eq. 6}$$

where RSS_1 and RSS_2 refer to the residual sum of squares from the lower order (fewer compartments or parameters) model and higher order model respectively, P_1 and P_2 are the number of parameters in the two model configurations and N is the number of data points in the kinetic sequence.

This statistic applied to the usable 150 planes of dynamic

data in the 11 normal controls resulted in a significant improvement in data fit with the three- compared to two-compartment models ($p < 0.01$) and a trend in improvement that did not reach statistical significance when comparing the three compartment model with a tissue vascular space component (28) added to the basic three-compartment model ($0.05 < p < 0.1$).

Parameter Estimates

Table 1 A-B includes the results of the parameter estimates for K_1 , k_2 , k_3 and k_4 using the three-compartment model in the 11 normal controls. Additionally included are calculated values for K_{NLR} , K_{PAT} , $t_{1/2}(C_e)$ and $t_{1/2}(C_b)$ for the same patient group. K_{PAT} values were obtained from parametric images generated as described above, using the same regions of interest as employed in the nonlinear regression analysis.

Also included in Tables 1 A-B are the parameter results for the three subjects who underwent rapid initial scanning and had resultant input functions extracted from the image data. The data for these subjects are displayed with, and without, a correction for the plasma/left ventricular concentration gradient derived from Figure 3.

Figure 4 is a representative set of time-activity data obtained with a directly measured plasma input function illustrating the good statistical quality of the data and model fit using nonlinear regression and the three compartment model.

Figure 5 is a representative Patlak plot from a normal vertebral body ROI illustrating the high quality of the linear fit to the data.

Figure 6 is a plot of the average values of K_{NLR} versus K_{PAT} obtained from Table 1. Linear regression yielded a slope of 0.92 and a correlation coefficient of 0.95.

Figure 7 contains a plot of K_{PAT} from a single subject at each image plane, together with values of the average peak and minimum values of K_{PAT} for the normal group.

Mass Transport and Plasma Concentration of Fluoride

Plasma fluoride samples for the three normal subjects and the breast cancer patient were all within the normal range ($15 \mu\text{mol/liter}$). From Equation 2, it is evident that the mass flux of fluoride transport is directly related to K_{NLR} (or K_{PAT}) and the plasma fluoride concentration. The fluoride flux values (nmol/min/ml), expressed in terms of a minimum, maximum and average value for the 15 image planes in the studies are listed in Table 2 for the three normal subjects and the two studies of the cancer patient in whom plasma fluoride was assayed.

Parametric Images in Normal Subjects and Cancer Patients

Figure 8 illustrates summed images from a dynamic sequence together with a single image frame and a parametric image of K_{PAT} from a normal control subject. Parametric images of K_{PAT} were generated for each usable image plane in all subjects.

TABLE 1A
Three-Compartment Model Parameters

Subject no.	K ₁ ml/min/ml	k ₂ min ⁻¹	k ₃ min ⁻¹	k ₄ min ⁻¹	BV [†] ml/ml	t _{1/2} (e) min	t _{1/2} (b) hrs	K _{NLR} ml/min/ml	K _{PAT} ml/min/ml
Using Plasma Input									
1	0.0870 [0.0157] [‡]	0.1204 [0.1045]	0.0789 [0.0412]	0.0007 [0.0004]	0.2237 [0.0909]	5.22 [3.46]	24.2 [14.5]	0.0374 [0.0060]	0.0389 [0.0060]
2	0.1044 [0.0419]	0.3455 [0.2472]	0.1355 [0.0676]	0.0005 [0.0005]	0.0274 [0.0252]	1.94 [1.11]	64.7 [133.1]	0.0292 [0.0067]	0.0278 [0.0056]
3	0.0773 [0.0254]	0.1704 [0.0915]	0.1629 [0.0502]	0.0019 [0.0033]	0.0272 [0.0214]	2.41 [0.98]	16.5 [12.7]	0.0379 [0.0065]	0.0360 [0.0060]
4	0.0975 [0.1106]	0.2741 [0.4252]	0.1176 [0.1131]	0.0034 [0.0094]	0.1407 [0.0657]	3.92 [2.79]	53.2 [67.7]	0.0263 [0.0050]	0.0265 [0.0051]
5	0.0743 [0.0202]	0.1738 [0.1917]	0.1201 [0.1191]	0.0026 [0.0038]	0.1087 [0.0468]	9.33 [11.71]	19.1 [19.5]	0.0315 [0.0093]	0.0352 [0.0063]
6	0.2647 [0.2202]	0.6850 [0.6546]	0.1597 [0.0992]	0.0017 [0.0048]	0.0109 [0.0177]	3.83 [8.27]	379.2 [726.9]	0.0430 [0.0123]	0.0403 [0.0068]
7	0.0953 [0.0281]	0.2162 [0.1455]	0.1200 [0.0716]	0.0034 [0.0046]	0.0358 [0.0300]	3.12 [2.08]	30.3 [34.3]	0.0343 [0.0085]	0.0313 [0.0071]
8	0.0937 [0.0265]	0.1785 [0.1951]	0.0978 [0.1090]	0.0019 [0.0046]	0.0328 [0.0258]	5.76 [4.09]	27.5 [36.4]	0.0345 [0.0078]	0.0343 [0.0078]
9	0.1020 [0.0271]	0.1437 [0.1288]	0.1227 [0.1104]	0.0022 [0.0029]	0.1011 [0.0505]	4.39 [3.00]	21.6 [23.3]	0.0479 [0.0084]	0.0472 [0.0070]
10	0.0711 [0.0282]	0.2168 [0.1940]	0.1810 [0.0826]	0.0004 [0.0004]	0.0431 [0.0515]	2.38 [1.53]	47.4 [36.7]	0.0323 [0.0046]	0.0321 [0.0043]
11	0.0990 [0.0589]	0.3128 [0.5789]	0.1525 [0.1330]	0.0037 [0.0064]	0.1142 [0.0673]	4.82 [4.17]	31.3 [42.5]	0.0414 [0.0056]	0.0411 [0.0022]
Ave 1–11	0.1060	0.2579	0.1317	0.0020	0.0787	4.28	65.0	0.0360	0.0355
s.d.	[0.0539]	[0.1580]	[0.0302]	[0.0012]	[0.0653]	[2.08]	[105.3]	[0.0064]	[0.0061]
Ave 9–11	0.0907	0.2244	0.1521	0.0021	0.0861	3.86	33.4	0.0405	0.0401
s.d.	[0.0170]	[0.0848]	[0.0292]	[0.0017]	[0.0378]	[1.30]	[13.0]	[0.0078]	[0.0076]

* Subjects 1–8 had a lower frequency scanning sequence, and subjects 9–11 had higher frequency scanning sequence (see Methods).

[†] BV = blood volume.

[‡] Standard deviations are in brackets.

TABLE 1B
Three-Compartment Model Parameters

Subject no.	K ₁ ml/min/ml	k ₂ min ⁻¹	k ₃ min ⁻¹	k ₄ min ⁻¹	BV [†] ml/ml	t _{1/2} (e) min	t _{1/2} (b) hrs	K _{NLR} ml/min/ml	K _{PAT} ml/min/ml
Using LV Cavity Input (without P/LV Correction)									
9	0.1223 [0.0463] [‡]	0.0834 [0.1100]	0.0779 [0.0747]	0.0047 [0.0077]	0.0605 [0.0493]	8.75 [5.65]	11.9 [12.2]	0.0600 [0.0136]	0.0612 [0.0085]
10	0.1303 [0.0711]	0.2945 [0.2394]	0.1699 [0.0886]	0.0008 [0.0010]	0.0408 [0.0732]	2.42 [1.84]	60.5 [114.0]	0.0477 [0.0066]	0.0467 [0.0063]
11	0.1305 [0.0545]	0.2050 [0.2270]	0.1224 [0.0895]	0.0006 [0.0006]	0.0410 [0.0409]	4.40 [3.39]	32.6 [57.8]	0.0524 [0.0049]	0.0533 [0.0027]
Ave 9–11	0.1277	0.1943	0.1234	0.0020	0.0474	5.19	35.0	0.0534	0.0537
s.d.	[0.0047]	[0.1060]	[0.0460]	[0.0023]	[0.0113]	[3.24]	[24.4]	[0.0062]	[0.0073]
Using LV Cavity Input (with P/LV Correction)									
9	0.1291 [0.0931]	0.3533 [0.5456]	0.1570 [0.1295]	0.0068 [0.0069]	0.0337 [0.0324]	6.13 [7.98]	9.5 [12.0]	0.0471 [0.0120]	0.0428 [0.0059]
10	0.1420 [0.1706]	0.6974 [1.3224]	0.1682 [0.0879]	0.0005 [0.0011]	0.0175 [0.0300]	2.27 [1.85]	96.9 [291.5]	0.0331 [0.0043]	0.0327 [0.0044]
11	0.1397 [0.1528]	0.5252 [0.8096]	0.1558 [0.1492]	0.0042 [0.0078]	0.0252 [0.0307]	3.83 [3.26]	33.3 [41.0]	0.0377 [0.0090]	0.0373 [0.0019]
Ave 9–11	0.1369	0.5253	0.1603	0.0038	0.0255	4.08	46.5	0.0393	0.0376
s.d.	[0.0069]	[0.1721]	[0.0068]	[0.0032]	[0.0081]	[1.94]	[45.2]	[0.0071]	[0.0051]

* Subjects 1–8 had lower frequency scanning sequence, and subjects 9–11 had higher frequency scanning sequence (see Methods).

[†] BV = blood volume.

[‡] Standard deviations are in brackets.

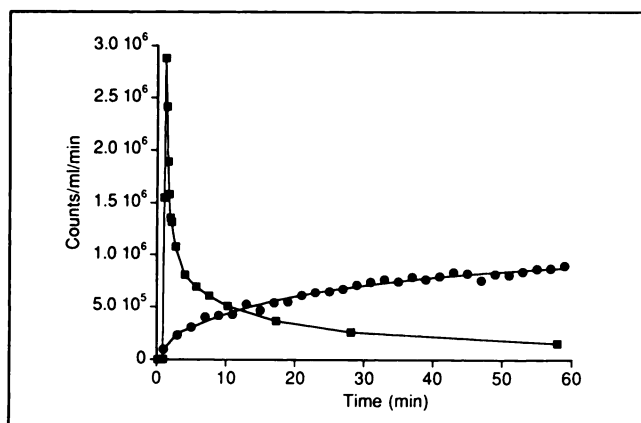


FIGURE 4. Representative plasma input function (filled squares) and vertebral body ^{18}F concentrations obtained from a normal volunteer in a 60-min acquisition sequence. Filled circles are bone ^{18}F concentrations for each image, while the smooth line through the data is the three compartment model fit to the data. A smooth line (interpolation) was drawn through the input function data to illustrate the shape of the curve.

Figure 9 is a parametric image of K_{PAT} from the breast cancer patient, illustrating a focal zone of increased uptake corresponding to metastatic disease in the neural arch.

DISCUSSION

Fluorine-18-fluoride Ion Distribution Between Plasma and Whole Blood

Figures 2 and 3 demonstrate that ^{18}F fluoride ion does not distribute homogeneously between plasma and red blood cells, and is consistent with a higher concentration of ^{18}F fluoride ion in plasma than red blood cells as previously noted by Hosking and Chamberlain (32) and Charkes et al. (14). Therefore, an input function obtained from arterialized venous plasma samples will be consist-

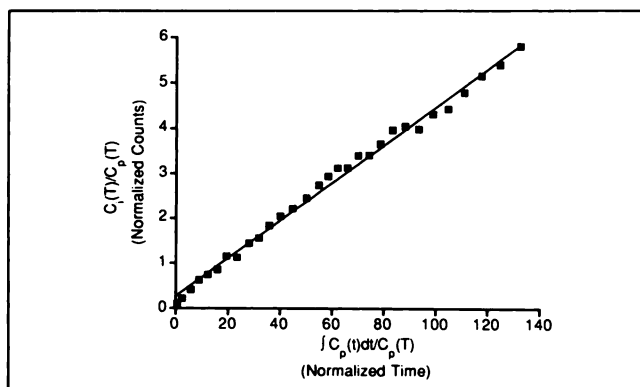


FIGURE 5. Representative Patlak plot, determined by plotting normalized time $\left(\int_0^T [C_p(t) dt] / C_p(T) \right)$ versus normalized counts $(C_t(T)/C_p(T))$ from a normal volunteer using the same data illustrated in Figure 4. Filled squares are data points, while the straight line is a linear fit to the data (which yields the value of K_{PAT}). For this example, the correlation coefficient is 1.00.

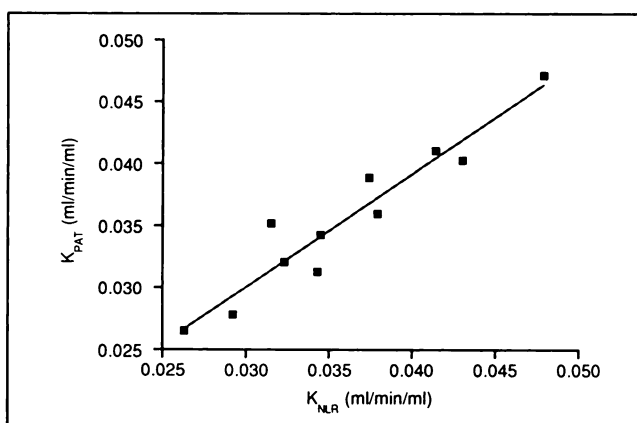


FIGURE 6. Plot of the average values of K_{NLR} versus K_{PAT} for all image planes in each of 11 normal volunteers. The straight line is a linear regression fit to the data: $y = 0.0025 + 0.92x$; the correlation coefficient is 0.95.

ently larger in magnitude than an input function obtained from whole blood samples or from a left ventricular ROI on a dynamic image set. This factor must be considered when generating kinetic estimates of the model parameters.

The higher ratio of plasma-to-left ventricular counts compared to plasma-to-whole blood activity (Fig. 3) is consistent with partial volume effects on the measured left ventricular input function. Because there is essentially no extraction of ^{18}F fluoride ion by the myocardium, the partial volume effect will decrease the measured ventricular cavity activity without any compensating spillover from the myocardium into the left ventricular ROI. Additionally, the relative impact of partial volume averaging upon the measured left ventricular ROI will be affected by the scan level: image planes closer to the superior or inferior margins of the left ventricle will result in a correspondingly greater averaging of myocardial tissue (low counts) in the measured input function data.

Another factor contributing to differences between input functions derived from image data versus that from peripheral arterial or venous blood is the temporal separation between input functions measured in different locations of the body. For example, the transit time for a bolus of activity traveling from the heart to an arterialized vein in the hand is on the order of 10 to 30 sec, depending on patient size, circulation time and other factors. Additionally, dispersion effects will alter the shape of a peripherally measured bolus. Unlike organs with a spatially defined vascular input, such as the brain, the skeletal system has a distributed network of vascular inputs. It is therefore necessary to be consistent in defining the measured input function for skeletal kinetic studies. In the absence of a true local measurable input function, employing a central input function derived from the heart or peripheral vascular site is appropriate if the implications of the above effects are considered in interpreting the data.

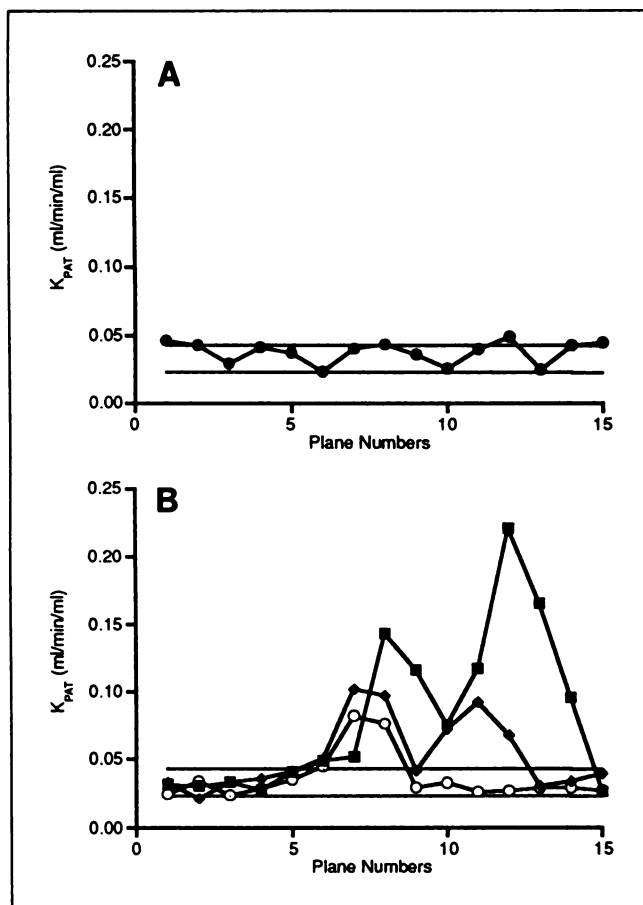


FIGURE 7. Plot of K_{PAT} in a representative normal volunteer (A) at each of 15 image planes in a dynamic sequence (above), and in the breast cancer patient studied sequentially (B). In (A), the solid lines represent the average minimum and maximum K_{PAT} values from the control group, while the filled circles connected by straight lines are the results from a single subject. Note the expected sinusoidal variation of K_{PAT} across the image planes because of the periodic distribution of vertebral bodies (high K_{PAT} values), and vertebral disk interspaces (low K_{PAT} values). In (B), the normal ranges are again illustrated, together with K_{PAT} values from the breast cancer patient studied initially (open circles), 4 mo later (filled squares) and 6 mo later (filled diamonds). Note the progressive changes in the K_{PAT} values over a range of scan levels.

Comparison of Two-Compartment Versus Three-Compartment Model

While the biological distribution of fluoride and its eventual incorporation into the hydroxyapatite crystal involves a sequence of steps, a goal of a kinetic model is to characterize a process in a simple, and kinetically identifiable, manner. In this sense, kinetic models are of necessity simplifications of the underlying biological system, but the modeling approach also is testable in terms of adequacy of model fits to the data from a statistical perspective. With these principles in mind, both a simple two-compartment and three-compartment model potentially can characterize [^{18}F]fluoride ion uptake in bone.

The three-compartment model is the preferred config-

uration compared to the two-compartment model based upon the F statistic comparison ($p < 0.01$). Adding a tissue vascular space to the three-compartment model marginally improved the quality of the fit to the data ($0.05 < p < 0.1$), but, as we have previously demonstrated with FDG cerebral kinetic studies, it is an effective way of accounting for nonextracted tracer remaining within the tissue vascular space (28). The tissue vascular compartment in this model probably primarily reflects nonextracted activity in marrow vessels, rather than bone blood volume per se.

The estimated average blood volume in vertebral bodies of normal subjects in this study ranged from 0.0255 ml/ml in the three volunteers with left ventricular input functions corrected for plasma/left ventricular activity gradients to 0.0787 ml/ml for the group of 11 volunteers using directly measured plasma input functions (Table 1). These values compare to values of 0.050 ml/ml bone in dog trabecular bone (33). While the bone vascular volume will be significantly higher in trabecular bone compared to cortical bone, the estimate obtained in this study appears to fall within a physiologically acceptable range, and supports a three-compartment model configuration, including a tissue vascular compartment. The variability in the estimated values of the vascular volume illustrate the relative sensitivity of this microparameter to the processing technique. While adding this term to the model is advantageous for the reasons discussed above, caution must be employed when interpreting the significance of its absolute value in a given subject.

Parameter Estimates

The results in Table 1 and Figure 6 indicate that there is a very good correspondence between K_{NLR} and K_{PAT} , both for the initial rapidly and more slowly imaged data set (0.0360 ± 0.0064 ml/min/ml for K_{NLR} in the 11 subjects with plasma input functions compared to 0.0355 ± 0.0061 ml/min/ml for K_{PAT} using plasma input functions). These values are also in good agreement with those obtained with plasma/left ventricular concentration gradient corrected left ventricular input functions (see Table 1).

The individual model microparameters reveal a good level of consistency across the normal population, while also indicating some sensitivity to the method employed in measuring the input function.

The average half-times for turnover of the fluoride ion in the extravascular compartment C_e (4.28 ± 2.08 min for plasma input function group of 11 subjects) and turnover of bound fluoride (65.0 ± 105.3 hr) are consistent with the relatively rapid uptake of [^{18}F]fluoride ion in the bound space within bone, and its slow rate of release from that compartment. Clearly, with a dynamic study of only 1 hr duration, one cannot make an accurate measurement of the turnover time in the C_b compartment when it appears to be very much longer than the time period of observation. It is apparent, however, that the turnover rate in the bound compartment is much slower than in the C_e com-

TABLE 2
Fluoride Flux Values

Subject no.	Plasma F ($\mu\text{mol/liter}$)	Min K_{PAT}^*	Max K_{PAT}	Ave K_{PAT} (ml/min/ml)	Min K(F)	Max K(F)	Ave K(F) (nmol/min/ml)
9	4.1	0.0357	0.0569	0.0472 [0.0070] [†]	0.1463	0.2333	0.1935 [0.0287]
10	3.4	0.0224	0.0354	0.0321 [0.0043]	0.0762	0.1204	0.1091 [0.0146]
11	2.3	0.0377	0.0433	0.0411 [0.0022]	0.0867	0.0996	0.0945 [0.0051]
Ca-1 [‡]	1.6	0.0264	0.2212	0.0819 [0.0598]	0.0422	0.3539	0.1310 [0.0957]
Ca-2	3.3	0.0215	0.1023	0.0530 [0.0266]	0.0710	0.3376	0.1749 [0.0878]

* Min, Max and Ave K_{PAT} refer to minimum, maximum, and average values for K_{PAT} for the entire 15-plane sequence in each volunteer or patient study.

[†] Standard deviations are in brackets.

[‡] Ca-1 and Ca-2 are two different studies for the breast cancer patient.

partment. Additionally, the small absolute values of k_4 are consistent with the slow turnover time in the bound compartment and indicate that the assumption of a zero value for this parameter in the Patlak graphical analysis is reasonable. This assumption is further supported by the good agreement between K_{NLR} and K_{PAT} .

Previous investigations have indicated that there is a high initial extraction fraction of [^{18}F]fluoride ion in its transit through the bone (6,15). If this extraction approaches 100%, then K_1 should approximate bone blood flow. The average value of K_1 of 0.1060 ± 0.0539 ml/min/ml for the volunteers with plasma sampled input functions is in the same range as estimated cortical and trabecular bone blood flow rates in dogs of 0.05 ml/min/g and 0.16 ml/min/100 g, respectively (34). Our PET results are expressed per unit volume, rather than per unit weight, because our measurement of count densities in the image data is a volumetric measurement. However, correcting the above range of K_1 values for a bone density factor of about 1.4 g/ml (35) results in an average K_1 value of 0.0757 ml/min/g, also within the physiologic range of animal flow estimates.

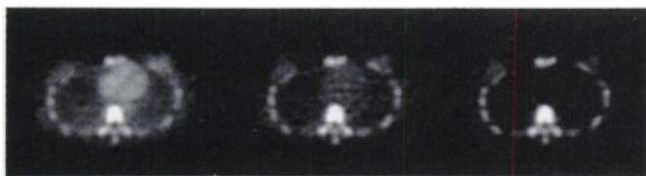


FIGURE 8. Example of a summed series of dynamic images from 3 to 60 min after injection (left), a single image frame at 60 min after injection (middle) and a parametric image of K_{PAT} (right). The summed image illustrates a significant amount of activity within the heart chambers (note the interventricular septum), which is less evident on the single frame image (middle). Note the further suppression of vascular activity on the parametric image (right).

Our estimates of K_1 are higher than estimates of skeletal blood flow in humans obtained by Reeve et al. (17) with a [^{18}F]fluoride ion plasma clearance technique. As discussed by those authors, however, their plasma clearance method may underestimate skeletal blood flow. Additionally, their method produces an estimate of global average skeletal blood flow, which may not be representative of blood flow to the spine.

Because K_{NLR} and K_{PAT} describe net [^{18}F]fluoride ion uptake in bone and are relatively less affected by changes in individual transport rate constants, they are the most useful indices for quantitatively describing bone [^{18}F]fluoride ion uptake. K_{PAT} is a computationally convenient parameter for quantitative studies because it can be derived regionally from parametric images as discussed below.

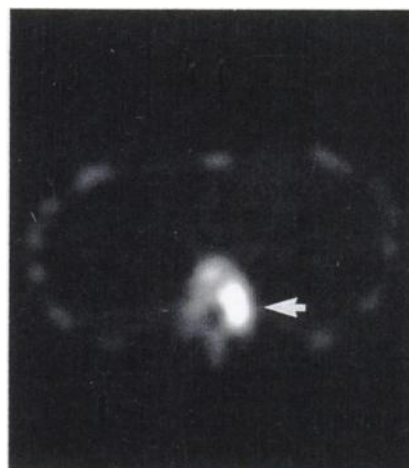


FIGURE 9. Parametric image of K_{PAT} through the mid-thoracic spine in a breast cancer patient. The arrow identifies increased uptake of [^{18}F]fluoride caused by metastatic disease in the left neural arch. K_{PAT} for the abnormal neural arch was 0.0941 ml/min/ml and 0.0281 ml/min/ml for the normal neural arch.

Fluoride Plasma and Mass Flux Measurements

Table 2 indicates that in the limited number of subjects assayed in this series, the plasma fluoride levels were all within a relatively narrow range. The primary parameter of interest, related to mass transport, is therefore K_{NLR} or K_{PAT} , rather than the flux value per se. In clinical states where the plasma fluoride level may not be in the normal range (e.g., in fluoride therapy for osteoporosis or in other conditions) additional investigations of [^{18}F]fluoride ion kinetics may be helpful in characterizing the relationship between plasma fluoride concentrations and [^{18}F]fluoride ion transport between intra- and extravascular spaces, as well as incorporation into and removal from hydroxyapatite crystals.

Parametric Images in Normal Subjects and Cancer Patients

Parametric images of K_{PAT} are of high visual quality (Fig. 8) and, analogous to parametric images of myocardial glucose utilization with FDG (21), both facilitate regional quantification of tracer uptake and increase the signal-to-noise ratio of the images by suppressing signal from the vascular space in the final image.

The excellent correspondence between K_{NLR} and K_{PAT} indicates that parametric image maps of K_{PAT} will reliably describe the regional uptake of [^{18}F]fluoride ion in bone and, as shown in Figure 9, are potentially useful in objectively monitoring changes in bone metabolism of [^{18}F]fluoride ion over time in disease states.

CONCLUSION

PET evaluation of [^{18}F]fluoride ion kinetics permits regional quantification of fluoride ion uptake characteristics. A three-compartment model, as well as Patlak graphical analysis, yield consistent estimates of a rate constant for net uptake of [^{18}F]fluoride ion in bone. Parametric imaging of this "bone metabolic index" using a Patlak-based method facilitates regional quantification as well as tomographic imaging of [^{18}F]fluoride ion uptake in the skeletal system. Potential applications of this technique include objective evaluations of focal bone disease (e.g., malignancies) as well as generalized bone metabolic disorders where alterations in [^{18}F]fluoride ion kinetics may occur that, in the absence of formal quantification, are difficult to identify.

ACKNOWLEDGMENT

This work was supported in part by the Director of the Office of Energy Research, Office of Health and Environmental Research, Washington D.C.

REFERENCES

1. Fogelman I, Bessent RG, Turner JG, et al. The use of whole-body retention of Tc-99m-diphosphonate in the diagnosis of metabolic bone disease. *J Nucl Med* 1978;19:270-275.
2. Fogelman I, Bessent RG, Beasall G, et al. Estimation of skeletal involvement in primary hyperparathyroidism. *Ann Intern Med* 1980;92:65-67.
3. Front D, Israel O, Jerushalmi J, et al. Quantitative bone scintigraphy using SPECT. *J Nucl Med* 1989;30:240-245.
4. Israel O, Front D, Hardoff R, et al. In vivo SPECT quantitation of bone metabolism in hyperparathyroidism. *J Nucl Med* 1991;32:1157-1161.
5. Blau M, Nagler W, Bender MA. Fluorine-18: a new isotope for bone scanning. *J Nucl Med* 1962;3:332-334.
6. Van Dyke D, Anger HO, Yano Y, Bozzini C. Bone blood flow shown with ^{18}F and the positron camera. *Am J Physiol* 1965;209(1):65-70.
7. Dworkin HJ, Moon NF, Lessard RJ, LaFleur P. A study of the metabolism of fluorine-18 in dogs and its suitability for bone scanning. *J Nucl Med* 1966;7:510-520.
8. French RJ, McCready VR. The use of ^{18}F for bone scanning. *Br J Radiol* 1967;40:655-661.
9. Spencer R, Herbert R, Rish MW, Little WA. Bone scanning with ^{87}Sr , ^{89}Sr and ^{18}F . *Br J Radiol* 1967;40:641-654.
10. Weber DA, Greenberg EJ, Dimich A, Kenny PJ, Rothschild EO, Myers WPL, Laughlin JS. Kinetics of radionuclides used for bone studies. *J Nucl Med* 1968;10:8-17.
11. Harmer CL, Burns JE, Sams A, Spittle M. The value of fluorine-18 for scanning bone tumours. *Clin Radiol* 1969;20:204-212.
12. Blau M, Ganatra R, Bender MA. F-18 fluoride for bone imaging. *Semin Nucl Med* 1972;2:31-37.
13. Weber DA, Keyes JW, Landman S, Wilson GA. Comparison of $^{99\text{m}}\text{Tc}$ polyphosphate and ^{18}F for bone imaging. *Am J Roentgen, Rad Ther Nucl Med* 1974;121:184-190.
14. Charkes ND, Brookes M, Makler PT. Studies of skeletal tracer kinetics. II. Evaluation of a five-compartment model of [^{18}F]fluoride kinetics in rats. *J Nucl Med* 1979;20:1150-1157.
15. Wooton R, Dore C. The single-passage extraction of ^{18}F in rabbit bone. *Clin Phys Physiol Meas* 1986;7:333-343.
16. Wooton R, Reeve J, Spellacy E, Tellez-Yudilevich M. Skeletal blood flow in Paget's disease of bone and its response to calcitonin therapy. *Clin Sci Molec Med* 1978;54:69-74.
17. Reeve J, Arlot M, Wooton R, Edouard C, Tellez M, Hesp R, Green JR, Meunier PJ. Skeletal blood flow, iliac histomorphometry, and strontium kinetics in osteoporosis: a relationship between blood flow and corrected apposition rate. *J Clin Endocrinol Metab* 1988;66:1124-1131.
18. Charkes ND, Makler PT Jr, Phillips C. Studies of skeletal tracer kinetics. I. Digital computer solution of a five-compartment model of [^{18}F]fluoride kinetics in humans. *J Nucl Med* 1978;19:1301-1309.
19. Charkes ND. Skeletal blood flow: implications for bone-scan interpretation. *J Nucl Med* 1980;21:91-98.
20. Wieland BW, Bida GT, Padgett HC, Hendry GO. Current status of CTI target systems for the production of PET radiochemicals. Proceedings of the 3rd Workshop on Targetry and Target Chemistry, 19-23 June 1989, Vancouver, British Columbia, Canada.
21. Choi Y, Hawkins RA, Huang SC, et al. Parametric images of myocardial metabolic rate of glucose generated from dynamic cardiac PET and 2-[^{18}F] fluoro-2-deoxy-D-glucose studies. *J Nucl Med* 1991;32:733-738.
22. Weinberg IN, Huang SC, Hoffman EJ, et al. Validation of PET-acquired input functions for cardiac studies. *J Nucl Med* 1988;29:241-247.
23. Phelps ME, Huang SC, Hoffman EJ, Selin CJ, Sokoloff L, Kuhl DE. Tomographic measurement of local cerebral glucose metabolic rate in humans with (F-18)2-fluoro-2-deoxy-D-glucose: validation of method. *Ann Neurol* 1979;6:371-388.
24. Grynaps MD. Fluoride effects on bone crystals. *J Bone Min Res* 1990;5(suppl 1):S169-S175.
25. Hawkins RA, Phelps ME, Huang SC, et al. A kinetic evaluation of blood-barrier permeability in human brain tumors with ^{68}Ga EDTA and positron computed tomography. *J Cereb Blood Flow Metab* 1984;4:507-515.
26. Sokoloff L, Reivich M, Kennedy C, et al. The [^{14}C]deoxyglucose method for measurement of local cerebral glucose utilization: theory, procedure and normal values in the conscious and anesthetized albino rat. *J Neurochem* 1977;28:897-916.
27. Huang SC, Phelps ME, Hoffman EJ, Sideris K, Selin CJ, Kuhl DE. Noninvasive determination of local cerebral metabolic rate of glucose in man. *Am J Physiol* 1980;238:E69-E82.
28. Hawkins RA, Phelps ME, Huang SC. Effects of temporal sampling glucose metabolic rates, and disruptions of the blood-brain barrier on the FDG model with or without a vascular compartment: studies in human brain tumors with PET. *J Cereb Blood Flow Metab* 1986;6:170-183.
29. Patlak CS, Blasberg RG, Fenstermacher JD. Graphical evaluation of blood-to-brain transfer constants from multiple-time uptake data. *J Cereb Blood Flow Metab* 1983;3:1-7.
30. Patlak CS, Blasberg RG. Graphical evaluation of blood-to-brain transfer

constants from multiple-time uptake data. Generalizations. *J Cereb Blood Flow Metab* 1985;5:584-590.

31. Landaw EM, DiStefano JJ. Multiexponential, multicompartamental non-compartmental modeling. II. Data analysis and statistical considerations. *Am J Physiol* 1984;246:R665-R677.
32. Hosking DJ and Chamberlain MJ. Studies in man with ^{18}F . *Clin Sci* 1972;42:153-161.
33. Simonet WT, Bronk JT, Pinto MR, Williams EA, Meadows TH, Kelly PJ.

Cortical and cancellous bone: age-related changes in morphological features, fluid spaces, and calcium homeostasis in dogs. *Mayo Clin Proc* 1988;63:154-160.

34. Li G, Bronk, JT, Kelly PJ. Canine bone blood flow estimated with microspheres. *J Ortho Res* 1989;7:61-67.
35. Kalender WA, Felsenberg D, Louis O, et al. Reference values for trabecular and cortical vertebral bone density in single- and dual-energy quantitative computed tomography. *Eur J Rad* 1989;9:75-80.

SELF-STUDY TEST

Skeletal Nuclear Medicine

Questions are taken from the *Nuclear Medicine Self-Study Program I*, published by The Society of Nuclear Medicine

DIRECTIONS

The following items consist of a question or incomplete statement followed by five lettered answers or completions. Select the *one* lettered answer or completion that is *best* in each case. Answers may be found on page 747.

1. The "flare" phenomenon in bone scintigraphy refers to which *one* of the following?
 - A. An increase in uptake in healing metastases following therapy
 - B. The extended pattern seen with primary bone tumors.
 - C. The flame-like edge seen in long-bone lesions of Paget's disease.
 - D. The persisting minimal uptake seen in regressing metastases.
 - E. The calvarial flame seen in the skull on oblique views.
2. Which *one* of the following mechanisms is most important in causing locally increased uptake of a bone-seeking radiopharmaceutical in an osseous lesion?
 - A. Increased blood flow
 - B. Increased compact bone mass
 - C. The presence of excessive organic matrix
 - D. Increased local alkaline phosphatase activity
 - E. Increased surface area of hydroxyapatite crystals per unit volume of bone
3. A bone mineral measurement on the lumbar spine of a middle-aged woman was performed by dual-photon absorptiometry. Areal density was 0.75 g/cm^2 . This value is below the fracture threshold of 0.98 g/cm^2 and below the second percentile of the normal range, based on age, race, and sex-matched controls. The bone mineral image from which the quoted results were obtained is shown in Figure 1. Which *one* of the following statements regarding the interpretation of the bone mineral measurements in this patient is correct?
 - A. The bone mineral image shows evidence for significant degenerative disease.
 - B. The tracing shows some bone mineral in the location of the transverse processes. This invalidates the results and a radial bone mineral measurement should be used, instead, for evaluation of this patient.
 - C. Nearly all women with a bone mineral value of 0.75 g/cm^2 have one or more compression fractures.
 - D. The bone mineral measurement is likely to be of no clinical significance in this patient.
 - E. The bone mineral image shows uniform bone mineral distribution in the lumbar spine.

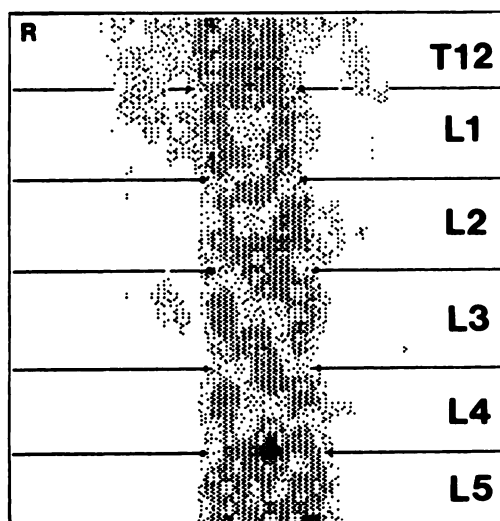
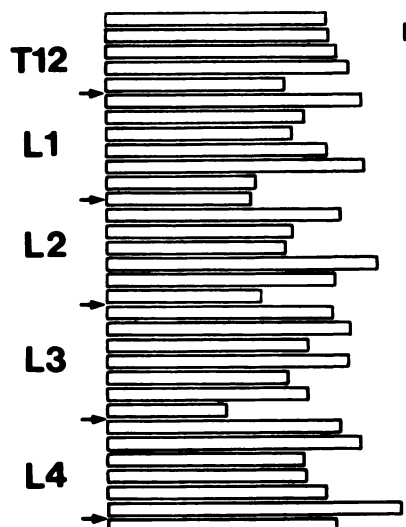


Figure 1



(continued on page 683)